Nanoscale

Accepted Manuscript

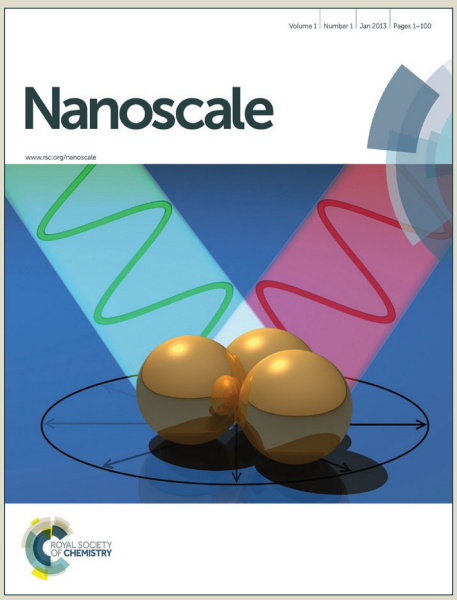

ROYAL SOCIETY OF CHEMISTRY

www.rsc.org/nanoscale

Au-nanocrystals-decorated δ-MnO_2 as efficient catalytic cathode for high-performance Li–O_2 batteries

Shuangyu Liu,[ab] Guoqing Wang,[a] Fangfang Tu,[a] Jian Xie,[*ac] Hui Ying Yang,[b] Shichao Zhang,[d] Tiejun Zhu,[a] Gaoshao Cao[c] and Xinbing Zhao[ac]

[a]*State Key Laboratory of Silicon Materials, School of Materials Science and Engineering, Zhejiang University, Hangzhou 310027, China. E-mail: xiejian1977@zju.edu.cn; Fax: +86-571-87951451; Tel: +86-571-87952181*
[b]*Pillar of Engineering Product Development, Singapore University of Technology and Design, 20 Dover Drive, Singapore 138682, Singapore*
[c]*Key Laboratory of Advanced Materials and Applications for Batteries of Zhejiang Province, Hangzhou 310027, China*
[d]*School of Materials Science and Engineering, Beijing University of Aeronautics and Astronautics, Beijing 100191, China*

†Electronic supplementary information (ESI) available: XPS of Au/δ-MnO_2, XRD of δ-MnO_2, nitrogen adsorption/desorption of Au/δ-MnO_2 on graphene-coated Ni foam, cycling stability of Li–O_2 battery with δ-MnO_2 catalyst, EIS of Li–O_2 battery with Au/δ-MnO_2 catalyst, and summary of electrochemical performance of Li–O_2 batteries with Mn-based or Au catalysts. See DOI:

Abstract

$Li–O_2$ battery works based on the reversible formation and decomposition of Li_2O_2, which is insulating and highly reactive. Designing catalytic cathode capable of controlling the Li_2O_2 growth recently becomes a challenge to overcome this barrier. In this work, we gave a new design of catalytic cathode by growing porous Au/δ-MnO_2 electrocatalyst directly on conductive substrate. We found that Au/δ-MnO_2 can catalyze the directed growth of Li_2O_2 into thin/small form, only inside porous δ-MnO_2, and along the surface of δ-MnO_2 sheets. We proposed the catalytic mechanism of Au/δ-MnO_2, where Au plays a critical role in catalyzing the nucleation, crystallization and conformal growth of Li_2O_2 on δ-MnO_2 sheets. $Li–O_2$ batteries with Au/δ-MnO_2 catalytic cathode show excellent electrochemical performance due to this favorable Li_2O_2 growth habit. The battery yields a high capacity of 10600 mAh g^{-1} with a low polarization of 0.91 V at 100 mA g^{-1}. Superior cycling stability can be achieved in both capacity-limited (500 mAh g^{-1}, 165 times at 400 mA g^{-1}) and unlimited (ca. 3000 mAh g^{-1}, 50 cycles at 800 mA g^{-1}) modes.

Introduction

$Li–O_2$ (Li–air) batteries can yield an energy density around 5–10 times higher than that of current Li-ion batteries (LIBs).[1–3] Despite recent advances in $Li–O_2$ batteries by optimizing the battery systems,[4–8] great challenges still remain to develop practical $Li–O_2$ batteries due to the sluggish oxygen reduction/evolution reaction (ORR/OER) kinetics in nonaqueous electrolyte.[9–12] The working of $Li–O_2$ batteries depends on the deposition/decomposition of insulating Li_2O_2 on cathode, in contrast to the Li ions shuttle mechanism between cathode and anode in LIBs. The cathode of $Li–O_2$ batteries will suffer from progressive deactivation and final death due to the accumulation of Li_2O_2 with a rather low electric conductivity.[13,14] Besides, Li_2O_2 or its intermediate (LiO_2) is highly reactive toward organic solvent (even for relatively stable 1,2-dimethoxyethane or DME),[15] carbon[16–18] and binder (e.g. polyvinylidene difluoride).[19] The accumulation of the byproducts, e.g. Li_2CO_3, also contributes to the passivation of the electrode.[16–18] Therefore, for the design of ideal catalytic cathodes, both catalyst component and electrode architecture should be considered.

The disadvantage of Li_2O_2 is expected to be partly relieved by growing it on conductive matrices. Recent reports have indicated that noble metal (Pd,[20] Pt[21], Ru[22], etc) inclusion in carbon matrix can catalyze the adhesion of Li_2O_2 onto the carbon matrix and crystallization of Li_2O_2 into low-dimensional forms (thin layer, small size, etc). In doing so, the deactivation of the electrode can be effectively alleviated or deferred, and the decomposition of Li_2O_2 can occur at low overpotentials upon recharge with reduced side reactions, for instance electrolyte oxidation.[23] Unfortunately, carbon materials are unstable in contact with Li_2O_2 (or LiO_2).[16–18] For this purpose, chemically/electrochemically more stable oxides have been suggested to replace carbon materials to support noble metals.[24,25]

In this work, we propose a new design of a catalytic cathode by growing porous Au-decorated δ-MnO_2 (Au/δ-MnO_2) directly on graphene-coated Ni foam (see Fig. 1). In this design, the use of binder is avoided and the carbon (graphene) is hidden underneath δ-MnO_2, excluding or minimizing the binder/carbon involved side reactions. Graphene introduction not only ensures uniform

deposition of δ-MnO_2 on Ni foam, but also increases electrode conductivity. MnO_2 is selected as the support for Au due to its superior catalytic activity for ORR and OER,[26–31] and is stable against the Li_2O_2 attack,[32] and porous δ-MnO_2 with a large surface area provides sufficient space for Li_2O_2 accommodation. Au plays an important role in catalyzing the directed oxygen reduction and Li_2O_2 growth into thin/small form, inside the porous δ-MnO_2, and along the δ-MnO_2 surface with the co-catalytic effect of δ-MnO_2. This favorable crystallization habit of Li_2O_2 enables excellent battery performance due to relieved electrode deactivation, easy Li_2O_2 decomposition, and reduced side reactions. The configuration and working mechanism of the Au/δ-MnO_2 catalytic cathode is schematically illustrated in Fig. 1.

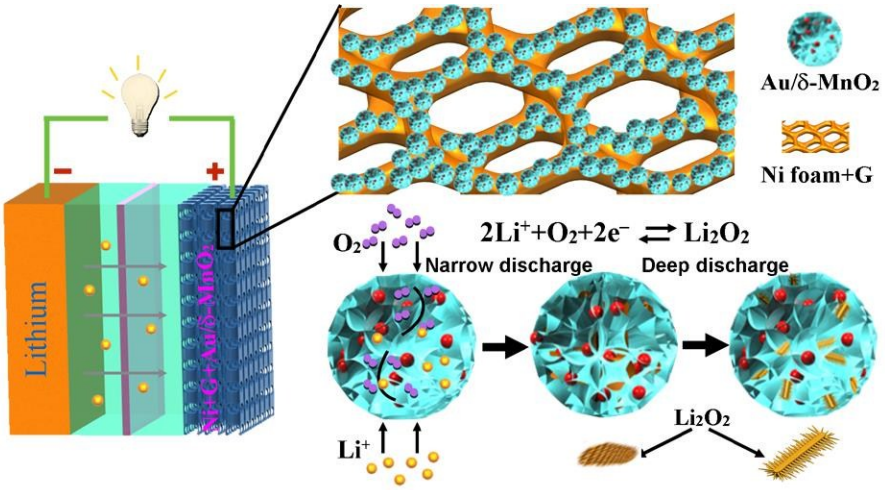

Fig. 1 Configuration and working mechanism of the Au/δ-MnO_2 catalytic cathode.

Experimental section

Synthesis of graphene on nickel foam

Porous nickel foam was used as the template to grow graphene by chemical vapor deposition (CVD) method. Nickel foam (density: ~285 g m^{-2}, thickness: ~1.6 mm, porosity: ≥96%, Heze Tianyu Technology Development Co., Ltd, China) was cut into pieces of 20 cm×5 cm and placed in a quartz tube of a horizontal tube furnace, followed by heating to 1000 °C at a rate of 50 °C min^{-1} under Ar/H_2 (4:1 in volume) at a flow rate of 1 L min^{-1} and holding at 1000 °C for 5 min to clean surface NiO. CH_4 at a flow rate of 10 mL min^{-1} was then carried into the tube furnace by the Ar/H_2

flow to grow graphene on the nickel foam. After reaction for 5 min at 1000 °C, the furnace was cooled down to room temperature at a rate of 100 °C min^{-1} under the Ar/H_2 flow. The loading of graphene on nickel foam is 0.63 mg cm^{-2}.

Synthesis of Au/δ-MnO_2 on graphene-coated Ni foam

To grow δ-MnO_2, the Ni foam coated with graphene was first put into a Teflon-lined stainless steel autoclave containing 0.01 M $KMnO_4$ (50 mL) and 96 wt% H_2SO_4 (20 μL), and maintained at 85 °C for 1 h. The Ni foam piece with deposit was then taken out from the autoclave, washed with distilled water repeatedly, and dried at 60 °C for 10 h in vacuum. After heating at 300 °C in Ar for 2 h, Ni foam supported δ-MnO_2 was obtained. The loading of δ-MnO_2 is 0.42 mg cm^{-2}. Ni foam supported Au/δ-MnO_2 was prepared by a solution impregnation method. Briefly, the Ni foam supported δ-MnO_2 was immersed in a $HAuCl_4 \cdot 3H_2O$ aqueous solution (4 mg mL^{-1}) at room temperature for 10 h, and then rinsed with distilled water and dried at 60 °C for 10 h in vacuum. The loading of Au is 0.22 mg cm^{-2}. The loadings of MnO_2 and Au were determined by weighing the electrode successively before and after deposition using a precise balance.

Materials characterization

The X-ray diffraction (XRD) patterns were obtained on a Rigaku D/Max-2550pc powder diffractometer with Cu K_α radiation (λ = 1.541 Å). X-ray photoelectron spectra (XPS) of the Ni foam supported Au/δ-MnO_2 electrode were recorded on a KRATOS AXIS ULTRA-DLD spectrometer with a monochromatic Al K_α radiation ($h\nu$ = 1486.6 eV). The morphologies of the electrodes or electrode components were observed by field-emission scanning electron microscope (SEM) on a FEI-sirion microscope and transmission electron microscopy (TEM)/high-resolution TEM (HRTEM) on a JEM 2100F microscope. N_2 absorption/desorption isotherms of 3D-G-Au/δ-MnO_2 on Ni foam were measured on an AUTOSORB-1-C apparatus.

Electrochemical measurements

Swagelok or coin-type Li–O_2 batteries were assembled in an argon-filled glove box using lithium metal as anode, Ni foam (with graphene coating) supported Au/δ-MnO_2 (or δ-MnO_2) as cathode (the area is 0.36 cm^2), and 0.1 M $LiClO_4$ in DME or 1 M $LiClO_4$ in tetraethylene glycol dimethyl ether (TEGDME) as electrolyte (water content <30 ppm). The electrodes were dried in a vacuum oven at 80 °C for 3 h before batteries assembly. The assembled batteries were purged with O_2 for 10 min and stayed at open voltage circuit (OCV) for 5 h prior to the electrochemical tests. Galvanostatic cycling was conducted on a Neware battery cycler (Shenzhen, China) over a voltage window of 2.0–4.5 V (vs. Li/Li^+). The specific capacity (mAh g^{-1}) and current density (mA g^{-1}) of the Au/δ-MnO_2 electrodes were calculated based on the total mass of δ-MnO_2 and Au. For the δ-MnO_2 electrode, the current density and specific capacity were calculated based on the mass of δ-MnO_2. Electrochemical impedance spectroscopy (EIS) measurements were performed on a Princeton Applied Research VersaSTAT3 electrochemistry workstation with an ac voltage of 10 mV amplitude over the frequency range 10^{-2}–10^5 Hz. All of the electrochemical measurements were performed at 25 °C.

Results and discussion

The preparation of the catalytic cathode is described in Experimental section. Fig. 2a shows the SEM image of graphene on Ni foam. The formed wrinkles indicate the intimate contact between Ni foam and graphene. The graphene grows only on the skeleton of Ni foam, inheriting its three-dimensional interconnected scaffold while its large pores were kept intact. As seen in Fig. 2b, the δ-MnO_2 grown on graphene-coated Ni foam exhibits a porous structure with a size around 5 μm. After solution impregnation, the porous δ-MnO_2 is decorated with small particles as shown in Fig. 2c,d. The decoration of Au particles on δ-MnO_2 sheets is more clearly seen by dark-field TEM (Fig. 2e). HRTEM reveals that a single Au particle consists of nanocrystals with a size below 5 nm (Fig. 2f). The lattice spacings of 0.24 and 0.20 nm correspond to the (111) and (200) planes of Au. Fig. 2g–j shows the dark-field TEM and the corresponding energy dispersive X-ray spectrometry (EDS)

mapping of Au-decorated δ-MnO_2. The results indicate that Au nanoparticles below 50 nm are uniformly decorated on the δ-MnO_2 nanosheets. The above characterization confirms the construction of Au/δ-MnO_2 on graphene-coated Ni foam. XPS (see Fig. S1 in the ESI†) analysis verifies that MnO_2 and Au were deposited on graphene-coated Ni foam, and XRD (see Fig. S2 in the ESI†) further verifies that the MnO_2 (exfoliated from the electrode before Au deposition) is δ-MnO_2. The 3D-G-Au/δ-MnO_2 electrode demonstrates a high Brunauer-Emmett-Teller (BET) surface area of 336 m^2g^{-1} (see Fig. S3 in the ESI†) due to its unique porous structure.

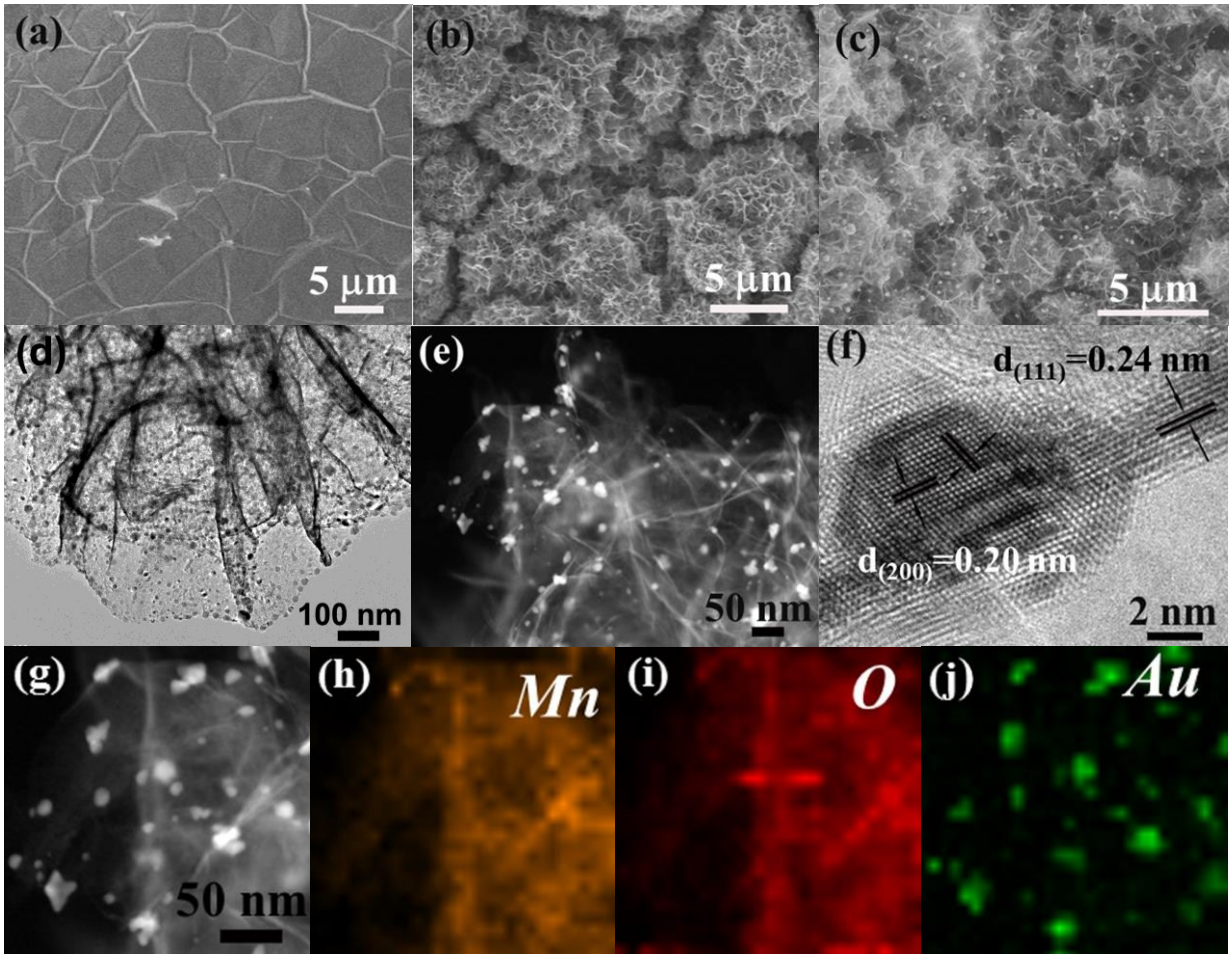

Fig. 2 Morphology and component analyses of Au/δ-MnO_2 on Ni foam. (a) SEM image of graphene on Ni foam, (b) SEM image of δ-MnO_2 on graphene, (c) SEM, (d) TEM and (e) dark-filed TEM images of Au-decorated δ-MnO_2, (f) HRTEM image of a single gold particle on δ-MnO_2, and (g–j) dark-filed TEM image and the corresponding EDS mapping of Au-decorated δ-MnO_2.

Li–O_2 batteries with δ-MnO_2 and Au/δ-MnO_2 cathodes were fabricated to investigate their

catalytic activity for ORR/OER. Fig. 3a compares the voltage profiles of Li–O_2 batteries catalyzed by δ-MnO_2 and Au/δ-MnO_2. The batteries were tested in 0.1 M $LiClO_4$/DME at 100 mA g^{-1}. For the Au/δ-MnO_2 electrode, the current density and specific capacity were calculated based on the total mass of Au and δ-MnO_2. For the δ-MnO_2 electrode, the current density and specific capacity were calculated based on the mass of δ-MnO_2. The mass of graphene was not included in the calculation of current density and specific capacity because we found that even the exposed graphene on Ni foam shows weak catalytic activity and it only acts as the conductive substrate,[26] while Ni itself also shows poor catalytic activity.[33] The Li–O_2 battery with Au/δ-MnO_2 catalyst can yield a capacity of 10600 mAh g^{-1}, which is much higher than that with δ-MnO_2 catalyst (7400 mAh g^{-1}). In addition, Li–O_2 battery with Au/δ-MnO_2 catalyst exhibits lower polarization for both charge and discharge than that with δ-MnO_2 catalyst, despite the fact that the former is loaded with more insulating Li_2O_2. It is clear that the performance improvement is closely related to the presence of Au, whose effects will be discussed below. The high catalytic activity could also be achieved by using nanostructured porous catalysts, such as cobalt-manganese oxide[34] and perovskite $LaNiO_3$.[35] Fig. 3b presents the discharge profiles of Au/δ-MnO_2 catalyzed Li–O_2 battery at various current densities. At 100 mA g^{-1} (0.064 mA cm^{-2}), the battery shows a rather high discharge plateau of 2.87 V, close to the reversible value (E_{rev} = 2.96 V) in nonaqueous Li–O_2 battery. Even at 1600 mA g^{-1} (1.024 mA cm^{-2}), the battery can still deliver a large discharge capacity (1935 mAh g^{-1}) and a high discharge plateau (~ 2.4 V) due to the excellent catalytic activity of Au/δ-MnO_2 for ORR.

The durability of the catalytic activity of Au/δ-MnO_2 catalyst was evaluated by repeated cycling of the Li–O_2 battery with Au/δ-MnO_2 catalytic cathode. The battery with Au/δ-MnO_2 cathode was first cycled under rigorous conditions: high current density of 800 mA g^{-1} (0.512 mA cm^{-2}), wide potential window (2–4.5 V), and no capacity limit. Under these conditions, severe electrode deactivation should occur by depositing large amounts of Li_2O_2. In addition, detrimental side reactions are easy to take place at a wide potential window. Interestingly, the Li–O_2 battery still

exhibits a good electrochemical performance in this charge/discharge mode. As seen in Fig. 3c, after 50 cycles, the capacity of the battery is maintained at 3012 mAh g^{-1}. In contrast, the Li-O_2 battery with δ-MnO_2 catalyst shows poor cycling stability (see Fig. S4 in the ESI†). The results indicate that Au/δ-MnO_2 is highly efficient for catalytic formation/decomposition of Li_2O_2, and that the side reactions are less significant than expected due to the unique design of the catalytic cathode.

The rate capability of the Au/δ-MnO_2 catalyzed Li–O_2 battery was also evaluated in capacity-limited mode (500 mAh g^{-1}) as seen in Fig. 3d. At a low current density of 100 mA g^{-1}, the battery exhibits a high discharge terminal potential of 2.92 V, close to the E_{rev} value of 2.96 V. At 1600 mA g^{-1}, the discharge terminal potential is still above 2.4 V, indicating superior catalytic performance of Au/δ-MnO_2 for ORR. The Au/δ-MnO_2 cathode is also highly efficient for OER especially at low current density (100–400 mA g^{-1}), where most of the Li_2O_2 can be decomposed below 4.0 V during charge.

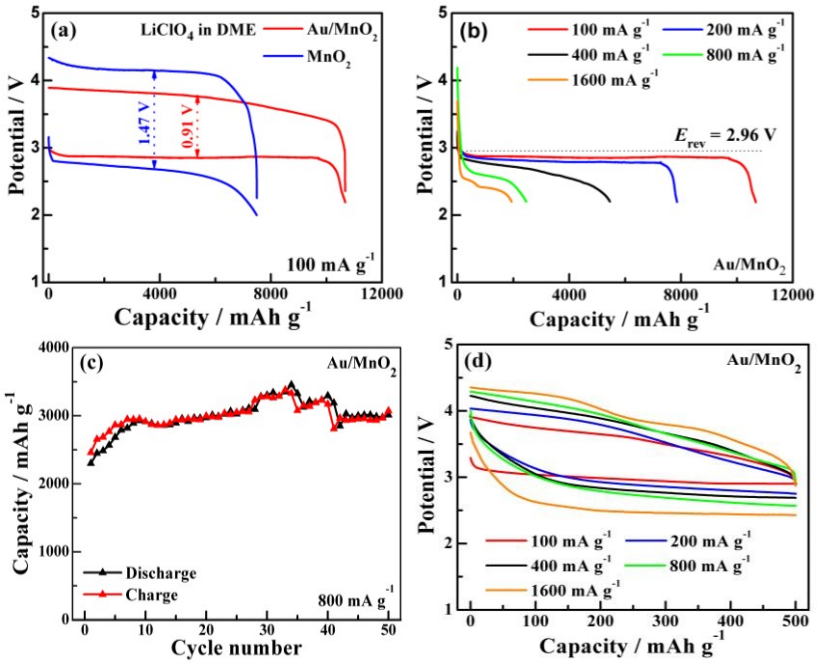

Fig. 3 Electrochemical performance of Li–O_2 batteries in 0.1 M $LiClO_4$/DME. (a) Comparison of voltage profiles of the batteries using Au/δ-MnO_2 and δ-MnO_2 catalysts at 100 mA g^{-1}, (b) discharge profiles of the battery using Au/δ-MnO_2 catalyst at various current densities, (c) cycling performance of the battery using Au/δ-MnO_2 catalyst at 800 mA g^{-1} between 2 and 4.5 V without

limiting the capacity, and (d) rate capability of the battery using Au/δ-MnO_2 catalyst with capacity limited at 500 mAh g^{-1}.

The durability of the catalytic activity of Au/δ-MnO_2 was evaluated by repeatedly cycling the Au/δ-MnO_2 catalyzed Li–O_2 batteries in capacity-limited mode. The batteries were first cycled in 0.1 M $LiClO_4$/DME at 400 mA g^{-1} (0.256 mA cm^{-2}) with the capacity limited at 500 mAh g^{-1} using swagelok-type cells (Fig. 4a–c). As seen in Fig. 4a, the discharge potential is maintained at a high value, while the charge potential is on the decrease during the initial cycles followed by a slight increase during the subsequent cycles. Fig. 4b shows the magnified view of the voltage profiles (marked area in Fig. 4a) during 50^{th}–100^{th} cycles, where the low polarization (maximum 0.65 V at 300 mAh g^{-1}) is evident due possibly to the gradual activation of catalytic cathode. Recently, Kang group has reported high-performance Li–O_2 batteries with rather low polarization and excellent cycling stability by using aligned carbon nanotubes cathode and soluble catalyst.[8] In our work, the low polarization and good cycling stability are attributed mainly to good catalytic activity of Au/δ-MnO_2 and the minimized exposure of carbon while still maintaining good electrode conductivity contributed by the hidden graphene. Fig. 4c exhibits the terminal voltage and discharge capacity with cycle number. During 100 cycles, the capacity can be maintained at 500 mAh g^{-1}. Besides, the terminal voltages of charge and discharge can be kept at around 4.0 and 2.6 V, respectively. This is desirable since some unfavorable parasitic reactions, such as that between Li_2O_2 (or LiO_2) and DME,[15,23] can be effectively inhibited when the battery is operated at a narrow potential window.

The durability of the catalytic activity of Au/δ-MnO_2 was also checked by long-term cycling in 1 M $LiClO_4$/TEGDME at 400 mA g^{-1} (0.256 mA cm^{-2}) using coin-type cells (with pores in cathode side) (Fig. 4d–f). In this case, TEGDME instead of DME was used since it is difficult to volatilize at room temperature. Similarly, the charge potential of the Li–O_2 battery with 1 M $LiClO_4$/TEGDME also shows a tendency to decrease after the initial cycles and increases gradually until 165^{th} cycle

(Fig. 4d). Fig. 4e shows the magnified view of the marked area in Fig. 4d. A low polarization is also observed on 50th–100th cycles in 1 M $LiClO_4$/TEGDME. The discharge capacity of 500 mAh g^{-1} can be kept up to 165 cycles (Fig. 4f). After that, capacity fade and polarization increase occur which are caused by accumulation of byproducts, for example Li_2CO_3,[23,26] which indicates that stable electrolyte should be developed for further performance improvement.[36,37]

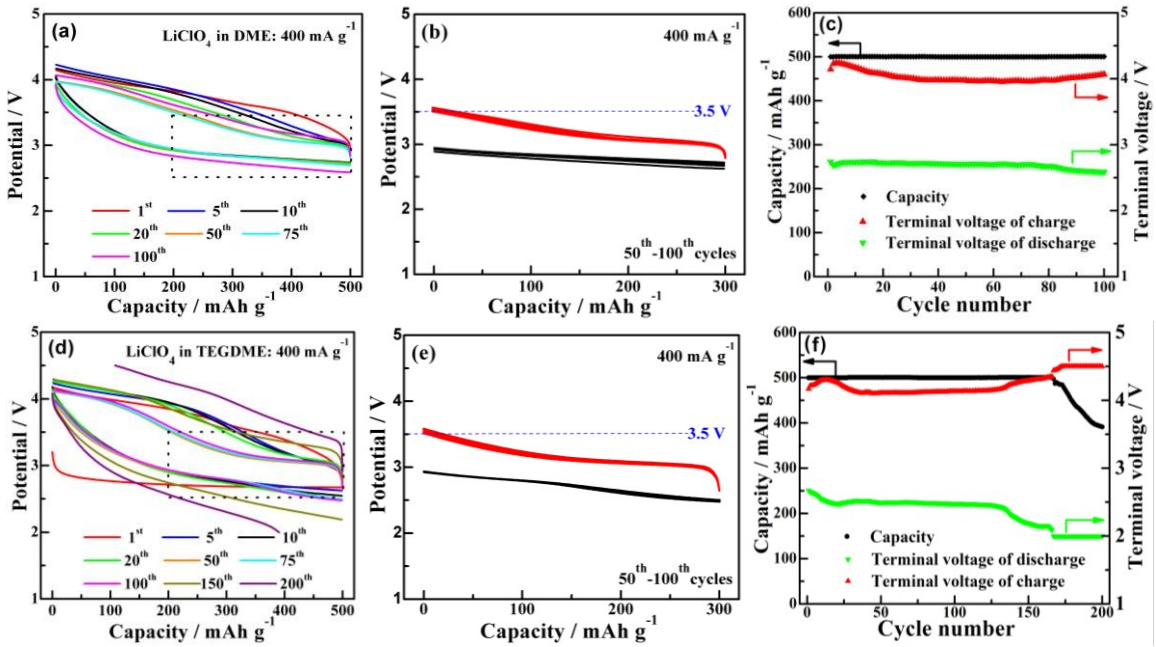

Fig. 4 Voltage profiles and cycling performance of Au/δ-MnO_2 catalyzed Li–O_2 batteries under 400 mA g^{-1} with the capacity limited at 500 mAh g^{-1}. (a–c) 0.1 M $LiClO_4$/DME using swagelok-type cells, and (d–f) 1 M $LiClO_4$/TEGDME using coin-type cells.

To reveal the superior catalytic activity of Au/δ-MnO_2 and the role that Au plays, the electrodes after discharge were observed by SEM and TEM. The loading of the SEM/TEM holders to the chamber was completed as quickly as possible to minimize the exposure of the sample to air. As shown in Fig. 5a, the porous structure is generally preserved after discharge to 1000 mAh g^{-1}. This means that Li_2O_2 forms only inside the porous δ-MnO_2. High-magnification image in Fig. 5d indicates that thin/small substance grows conformally along the surface of Au-decorated δ-MnO_2, and that the substance is rather thin since Au particles are still visible at this discharge state. In contrast, large micro-sized particles have formed on the δ-MnO_2 electrode after discharge to 1000 mAh g^{-1}, while the original porous structure is hardly seen (Fig. 6). The thin substance is further

revealed by TEM image in Fig. 5c and is confirmed to be Li_2O_2 by selected area electron diffraction (SAED, Fig. 5f). Good contact between Li_2O_2 and Au/δ-MnO_2 is thus anticipated since Li_2O_2 grows conformally on the surface of Au/δ-MnO_2 (Fig. 5c). Note than even after discharge to a high capacity of 5000 mAh g^{-1}, no large Li_2O_2 particles grow and only nanoscaled, dendritic Li_2O_2 can be seen (Fig. 5b,e). The dendritic Li_2O_2 is constructed by loosely stacked smaller nanoparticles. The deactivation of the air electrode will be alleviated or delayed by depositing thin/small or dendritic Li_2O_2 instead of large-sized Li_2O_2. Besides, the thin/small or dendritic Li_2O_2 with large surface area is kinetically easier to decompose upon recharge.[38–40] This can explain higher capacity and lower polarization of the Au/δ-MnO_2 catalyzed battery than the δ-MnO_2 catalyzed one and the excellent electrochemical performance of the Au/δ-MnO_2 catalyzed Li–O_2 batteries even operated in capacity-unlimited mode.

Clearly, the presence of Au nanoparticles catalyzes the directed crystallization of Li_2O_2 into thin/small or dendritic form and the conformal growth of Li_2O_2 along the surface of Au/δ-MnO_2 sheets. Based on the SEM and TEM results, we propose a possible catalytic mechanism of Au/δ-MnO_2 for the directed Li_2O_2 growth. Au nanoparticles can act both as the catalytic centers for ORR and as nucleation sites for Li_2O_2 crystallization at the beginning of the ORR due to its high oxygen adsorption energy.[41,42] Thus, the nucleation and crystallization of Li_2O_2 occur preferentially on Au than on δ-MnO_2. Once small Li_2O_2 grains have formed, they can act as the nucleation centers for the continuous Li_2O_2 growth under the catalytic effect of δ-MnO_2. The ability of δ-MnO_2 itself to act as the nucleation centers of Li_2O_2 growth will be dwarfed when the catalytically active Au is present. As the ORR proceeds, Li_2O_2 will grow along the surface of δ-MnO_2 sheets with the co-catalytic effects of Au and δ-MnO_2. Namely, conformal growth of thin/small Li_2O_2 on δ-MnO_2 sheets can be realized. At deeper discharge state, dendritic Li_2O_2 will form due possibly to the gradually weakened but still retained catalytic effect of Au/δ-MnO_2 with the accumulation of Li_2O_2. The unique structure of the catalytic electrode enables barrier-free transport of Li ion, electron and oxygen, and ensures the deposition of Li_2O_2 dominantly inside the porous δ-MnO_2. Without the

decoration of Au, δ-MnO_2 itself will serve as the catalytic sites for ORR and nucleation centers for Li_2O_2 growth at the very beginning of ORR. Therefore, Li_2O_2 will grow into large particles instead of thin/small form on the δ-MnO_2 sheets.

Similar phenomena were also observed in previous reports,[20–22] where noble metals also direct the growth of low-dimensional Li_2O_2 on the surface of carbon materials. In our case, this phenomenon is more attractive since the direct contract of carbon (graphene) with Li_2O_2 or LiO_2 is largely blocked by δ-MnO_2 which is chemically/electrochemically more stable against the attack of Li_2O_2 or LiO_2. This growth habit of Li_2O_2 on Au/δ-MnO_2 also facilitates catalytic decomposition of Li_2O_2. Reversible formation/decomposition of Li_2O_2 is thus expected as confirmed by EIS measurements (see Fig. S5 and Table S1 in the ESI†). The obvious increase in charge transfer resistance (R_{ct}) after discharge is ascribed to the deposition of insulating Li_2O_2. Upon recharge, the R_{ct} decreases considerably, indicating the sufficient decomposition of Li_2O_2. From Table S2 in the ESI, we can see that the electrochemical performance of our Li–O_2 batteries is among the best ones for Mn-based catalysts when comprehensively considering the capacity, cycle life, overpotentials and test conditions due to unique architecture and superior catalytic efficiency of the porous Au/δ-MnO_2 cathode.

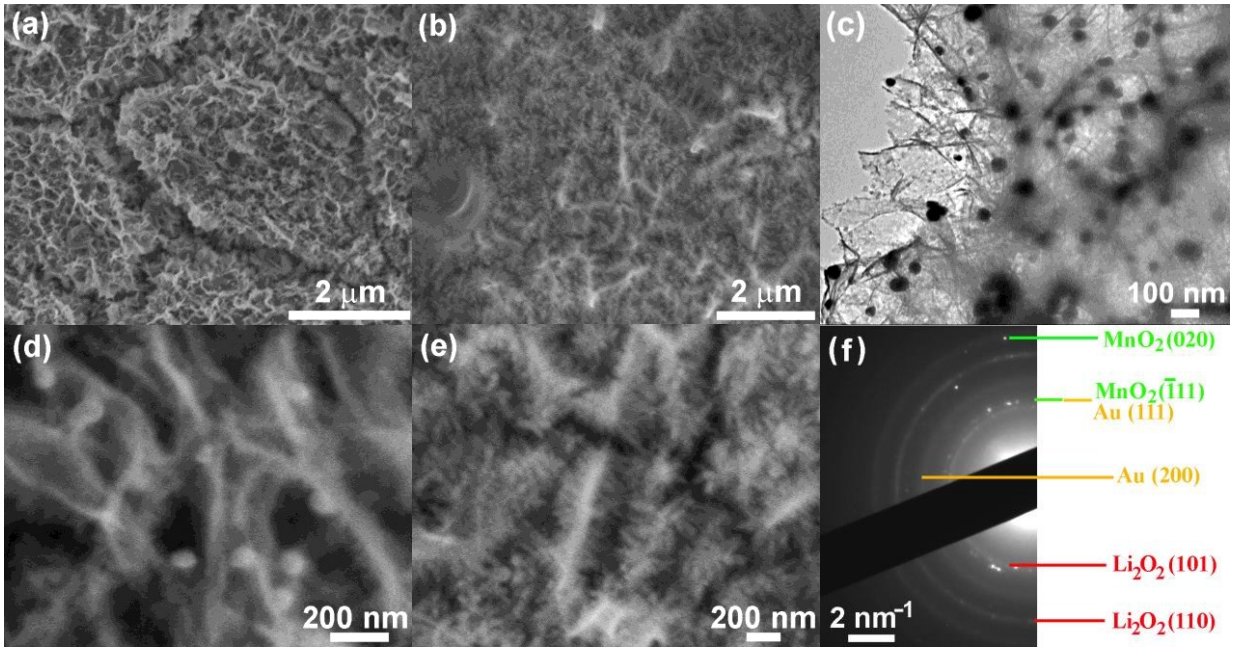

Fig. 5 Post cycling characterization of the Au/δ-MnO_2 electrode. (a,d) SEM images after discharge

to 1000 mAh g^{-1}, (b,e) SEM images after discharge to 5000 mAh g^{-1}, and (c) TEM image and (f) SAED patterns after discharge to 1000 mAh g^{-1}.

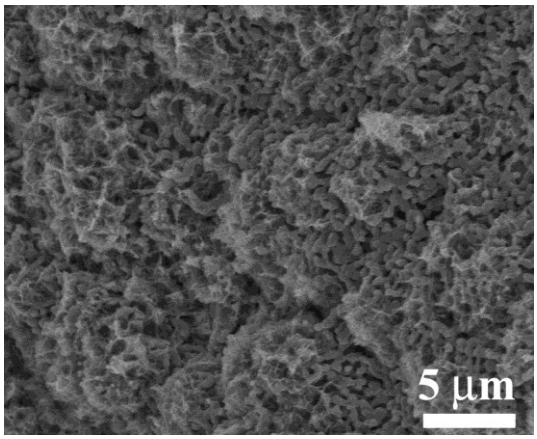

Fig. 6 SEM images of the δ-MnO_2 electrode after discharge to 1000 mAh g^{-1}.

Conclusions

In summary, we prepared binder-free porous Au/δ-MnO_2 catalytic electrode by growing Au-decorated δ-MnO_2 directly on graphene-coated Ni foam. In the Au/δ-MnO_2 catalytic cathode, Au acts both as catalytic centers for ORR and as nucleation/crystallization sites for Li_2O_2 growth at the beginning of ORR; As the ORR proceeds, the formed Li_2O_2 grains can serve as nucleation centers for the continuous growth of Li_2O_2 under the catalytic effect of δ-MnO_2; Finally, the conformal growth of thin/small Li_2O_2 on δ-MnO_2 is realized through the co-catalytic effects of Au and δ-MnO_2. Because of this controlled Li_2O_2 growth on chemically/electrochemically stable δ-MnO_2, Li–O_2 batteries with Au/δ-MnO_2 catalyst exhibit superior electrochemical properties. A large capacity of 10600 mAh g^{-1} and a high discharge plateau of 2.87 V at 100 mA g^{-1} can be achieved for the Au/δ-MnO_2 catalyzed batteries. When the capacity is limited at 500 mAh g^{-1}, the battery with Au/δ-MnO_2 catalyst can sustain 165 cycles at 400 mA g^{-1}. In the capacity-unlimited mode, a high capacity of 3012 mAh g^{-1} is retained after 50 cycles at 800 mA g^{-1}. The superior electrochemical performance of Li–O_2 batteries is due to the optimized design of catalytic electrode in both component and architecture.

Acknowledgements

This work was supported by the National Basic Research Program of China (2013CB934001), Zhejiang Provincial Natural Science Foundation of China under Grant No. Y15E010011, Key Science and Technology Innovation Team of Zhejiang Province under Grant Number 2010R50013, and Program for Innovative Research Team in University of Ministry of Education of China (IRT13037).

References

1 K. M. Abraham and Z. Jiang, *J. Electrochem. Soc.*, 1996, **143**, 1–4.

2 T. Ogasawara, A. Débart, M. Holzapfel, P. Novák and P. G. Bruce, *J. Am. Chem. Soc.*, 2006, **128**, 1390–1393.

3 P. G. Bruce, S. A. Freunberger, L. J. Hardwick and J. M. Tarascon, *Nat. Mater.*, 2012, **11**, 19–29.

4 H. G. Jung, J. Hassoun, J. B. Park, Y. K. Sun and B. Scrosati, *Nat. Chem.*, 2012, **4**, 579–585.

5 Z. Q. Peng, S. A. Freunberger, Y. H. Chen and P. G. Bruce, *Science*, 2012, **337**, 563–566.

6 J. J. Xu, D. Xu, Z. L. Wang, H. G. Wang, L. L. Zhang and X. B. Zhang, *Angew. Chem. Int. Ed.*, 2013, **52**, 3887–3890.

7 J. J. Xu, Z. L. Wang, D. Xu, F. Z. Meng and X. B. Zhang, *Energy Environ. Sci.*, 2014, **7**, 2213–2219.

8 H. D. Lim, H. Song, J. Kim, H. Gwon, Y. Bae, K. Y. Park, J. Hong, H. Kim, T. Kim, Y. H. Kim, X. Lepró, R. Ovalle Robles, R. H. Baughman and K. Kang, *Angew. Chem. Int. Ed.*, 2014, **53**, 3926–3931.

9 G. Girishkumar, B. McCloskey, A. C. Luntz, S. Swanson and W. Wilcke, *J. Phys. Chem. Lett.*, 2010, **1**, 2193–2203.

10 F. J. Li, T. Zhang and H. S. Zhou, *Energy Environ. Sci.*, 2013, **6**, 1125–1141.

11 F. Y. Cheng and J. Chen, *Chem. Soc. Rev.*, 2012, **41**, 2172–2192.

12 D. G. Kwabi, N. Ortiz Vitoriano, S. A. Freunberger, Y. Chen, N. Imanishi, P. G. Bruce and Y.

Shao Horn, *MRS Bull.*, 2014, **39**, 443–452.

13 V. Viswanathan, K. S. Thygesen, J. S. Hummelshøj, J. K. Nørskov, G. Girishkumar, B. D. McCloskey and A. C. Luntz, *J. Chem. Phys.*, 2011, **135**, 214704.

14 O. Gerbig, R. Merkle and J. Maier, *Adv. Mater.*, 2013, **25**, 3129–3133.

15 B. D. McCloskey, D. S. Bethune, R. M. Shelby, G. Girishkumar and A. C. Luntz, *J. Phys. Chem. Lett.*, 2011, **2**, 1161–1166.

16 B. D. McCloskey, A. Speidel, R. Scheffler, D. C. Miller, V. Viswanathan, J. S. Hummelshøj, J. K. Nørskov and A. C. Luntz, *J. Phys. Chem. Lett.*, 2012, **3**, 997–1001.

17 B. M. Gallant, R. R. Mitchell, D. G. Kwabi, J. G. Zhou, L. Zuin, C. V. Thompson and Y. Shao Horn, *J. Phys. Chem. C*, 2012, **116**, 20800–20805.

18 M. M. Ottakam Thotiyl, S. A. Freunberger, Z. Q. Peng and P. G. Bruce, *J. Am. Chem. Soc.*, 2013, **135**, 494−500.

19 R. Black, S. H. Oh, J. H. Lee, T. Yim, B. Adams and L. F. Nazar, *J. Am. Chem. Soc.*, 2012, **134**, 2902−2905.

20 J. J. Xu, Z. L. Wang, D. Xu, L. L. Zhang and X. B. Zhang, *Nat. Commun.*, 2013, **4**, 2438.

21 H. D. Lim, H. Song, H. Gwon, K. Y. Park, J. Kim, Y. Bae, H. Kim, S. K. Jung, T. Kim, Y. H. Kim, X. Lepró, R. Ovalle Robles, R. H. Baughmand and K. Kang, *Energy Environ. Sci.*, 2013, **6** 3570–3575.

22 E. Yilmaz, C. Yogi, K. Yamanaka, T. Ohta and H. R. Byon, *Nano Lett.*, 2013, **13**, 4679−4684.

23 B. D. McCloskey, D. S. Bethune, R. M. Shelby, T. Mori, R. Scheffler, A. Speidel, M. Sherwood and A. C. Luntz, *J. Phys. Chem. Lett.*, 2012, **3**, 3043−3047.

24 F. J. Li, D. M. Tang, Y. Chen, D. Golberg, H. Kitaura. T. Zhang, A. Yamada and H. S. Zhou, *Nano Lett.*, 2013, **13**, 4702−4707.

25 F. J. Li, D. M. Tang, Z. L. Jian, D. Q. Liu, D. Golberg, A. Yamada and H. S. Zhou, *Adv. Mater.*, 2014, **26**, 4659–4664.

26 S. Y. Liu, Y. G. Zhu, J. Xie, Y. Huo, H. Y. Yang, T. J. Zhu, G. S. Cao, X. B. Zhao and S. C.

Zhang, *Adv. Energy Mater.*, 2014, **4**, 1301960.

27 Y. Yu, B. Zhang, Y. B. He, Z. D. Huang, S. W. Oh and J. K. Kim, *J. Mater. Chem. A*, 2013, **1**, 1163–1170.

28 Y. Cao, M. S. Zheng, S. R. Cai, X. D. Lin, C. Yang, W. Q. Hu and Q. F. Dong, *J. Mater. Chem. A*, 2014, **2**, 18736–18741.

29 F. Y. Cheng, Y. Su, J. Liang, Z. L. Tao and J. Chen, *Chem. Mater.*, 2010, **22**, 898–905.

30 F. Y. Cheng, T. R. Zhang, Y. Zhang, J. Du, X. P. Han and J. Chen, *Angew. Chem. Int. Ed.*, 2013, **52**, 2474–2477.

31 K. Zhang, X. P. Han, Z. Hu, X. L. Zhang, Z. L. Tao and J. Chen, *Chem. Soc. Rev.*, 2015, **44**, 699–728.

32 R. Younesi, M. Hahlin, F. Björefors, P. Johansson and K. Edström, *Chem. Mater.*, 2013, **6**, 77–84.

33 Z. L. Wang, D. Xu, J. J. Xu, L. L. Zhang and X. B. Zhang, *Adv. Funct. Mater.*, 2012, **22**, 3699–3701.

34 J. Zhang, L. J. Wang, L. L. Xu, X. M. Ge, X. Zhao, M. Lai, Z. L. Liu and W. Chen, *Nanoscale*, 2015, **7**, 720–726.

35 J. Zhang, Y. B. Zhao, X. Zhao, Z. L. Liu and W. Chen, *Sci. Rep.*, 2014, **4**, 6005.

36 D. Xu, Z. L. Wang, J. J. Xu, L. L. Zhang and X. B. Zhang, *Chem. Commun.*, 2012, **48**, 6948–6950.

37 X D. Xu, Z. L. Wang, J. J. Xu, L. L. Zhang, L. M. Wang and X. B. Zhang, *Chem. Commun.*, 2012, **48**, 11674–11676.

38 M. D. Radin, J. F. Rodriguez, F. Tian and D. J. Siegel, *J. Am. Chem. Soc.*, 2012, **134**, 1093−1103.

39 M. D. Radina and D. J. Siegel, *Energy Environ. Sci.*, 2013, **6**, 2370–2379.

40 A. Dunst, V. Epp, I. Hanzu, S. A. Freunbergera and M. Wilkening. *Energy Environ. Sci.*, 2014, **7**, 2739–2752.

41 Y. C. Lu, H. A. Gasteiger and Y. Shao Horn, *J. Am. Chem. Soc.*, 2011, **133**, 19048–19051.

42 G. K. P. Dathar, W. A. Shelton and Y. Xu, *J. Phys. Chem. Lett.*, 2012, **3**, 891−895.

Table of contents entry

Porous Au/δ-MnO_2 on graphene-coated Ni foam exhibits superior catalytic effect for Li–O_2 batteries with Au-induced directed Li_2O_2 growth.